

In Silico Interpretation of cw-ESR at 9 and 95 GHz of Mono- and bis-TOAC-Labeled Aib-Homopeptides in Fluid and Frozen Acetonitrile

Silvia Carlotto,[†] Mirco Zerbetto,[†] Maryam Hashemi Shabestari,[‡] Alessandro Moretto,^{†,§} Fernando Formaggio,^{†,§} Marco Crisma,[§] Claudio Toniolo,^{†,§} Martina Huber,[‡] and Antonino Polimeno^{*†}

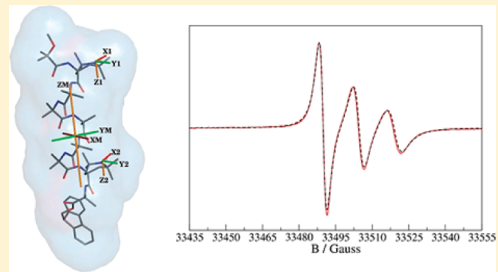
[†]Department of Chemistry, University of Padova, I-35131 Padova, Italy

[‡]Department of Molecular Physics, Leiden Institute of Physics, Leiden University, 2300 RA Leiden, The Netherlands

[§]Institute of Biomolecular Chemistry, CNR, Padova Unit, University of Padova, I-35131 Padova, Italy

 Supporting Information

ABSTRACT: In this paper, we address the interpretation of molecular properties of selected singly and doubly spin-labeled peptides from continuous-wave electron spin resonance (cw-ESR) spectroscopy. This study is performed by means of an integrated computational approach that merges a stochastic treatment of long-term dynamics to *ad hoc* methodologies for the calculation of structural properties. In particular, our method is based on (i) the determination of geometric and local magnetic parameters of the peptides by quantum mechanical density functional calculations by taking into account solvent contribution; (ii) the hydrodynamic evaluation of dissipative properties; and (iii) molecular dynamics including equilibrium distribution of molecular conformations. The system is then described by a stochastic Liouville equation in which the spin Hamiltonian for the two electron spins, interacting with each other and coupled to two ¹⁴N nuclear spins, is coupled to the diffusive operator describing the time evolution of slow coordinates. cw-ESR spectra are simulated for selected peptides built from the non-natural α -aminoacids α -aminoisobutyric acid (Aib) and 2,2,6,6-tetramethylpiperidine-1-oxyl-4-amino-4-carboxylic acid (TOAC). In particular, we study the —Aib—TOAC—Aib— singly labeled tripeptide and the —Aib—TOAC—(Aib)₇— singly labeled and —Aib—TOAC—(Aib)₅—TOAC—Aib— doubly labeled nonapeptides. We show that good agreement is obtained with minimal resorting to fitting procedures, proving that the combination of sensitive ESR spectroscopy and sophisticated modeling is a powerful approach to the investigation of both molecular dynamics and 3D-structural properties.



I. INTRODUCTION

Interpreting spectroscopic measurements and relating them to structural and dynamic properties and of molecular systems often requires a multiscale strategy, in which a coarse-grained treatment allows one to collect all the required relevant information to be used in the interpretation of suitable experimental observables. Tuning the frequency of the radiation interacting with matter offers the possibility to select the time-scales of motions to be observed. Also, quantities describing the radiation–matter interaction (e.g., Zeeman interaction in magnetic spectroscopies), especially when anisotropic, are very informative on the molecular structure, since they are strongly correlated to the electron density. An example is given by the site-directed spin labeling (SDSL) technique, combined with electron spin resonance (ESR) measurements, which is a promising approach to explore conformational transitions and detailed dynamical properties of peptides and proteins.^{1–3} SDSL is based on the covalent attachment of a stable nitroxide free radical to a reactive side-chain of an amino acid (e.g., cysteine) at selected sites along the polypeptide backbone. Spin labeling can be also carried out by synthetically including a non-natural α -aminoacid bearing a stable nitroxide moiety in the main-chain. To this end, a widely

employed spin label is 2,2,6,6-tetramethylpiperidine-1-oxyl-4-amino-4-carboxylic acid (TOAC).^{4–6} One of the main characteristics of TOAC is its ability to fold the peptide chain into a helical structure (3_{10} - or α -helix^{7,8}). This effect is related to the piperidine ring being rigidly attached to the backbone quaternary α -carbon. Multilabeling of peptides is an effective way to improve the investigation of both three-dimensional (3D)-structural information and internal dynamics via SDSL-ESR. When two or more spin labels are attached to the molecule, a set of experimental data is obtained showing higher complexity with respect to a singly labeled system. It includes the interaction among the spins giving access to their relative position, orientation, and dynamics. Thus, multilabeled systems can be used to infer structural parameters, such as the type of peptide secondary structure, and internal dynamics, if time-scales are compatible with the ESR relaxation frequencies.

ESR spectroscopy in the slow-motional regime can be interpreted following the stochastic Liouville equation (SLE) approach

Received: July 6, 2011

Revised: October 4, 2011

Published: October 4, 2011

developed by Freed and co-workers.^{9,10} It has been recently shown that the SLE approach can be linked profitably with advanced density functional theory (DFT) evaluation of geometry and magnetic parameters of the radical in its environment.¹¹ Dissipative parameters, such as rotational diffusion tensors, can in turn be determined at a mesoscopic level using standard hydrodynamic arguments.^{12–14} The combination of the evaluation of structural properties, based on quantum mechanical (QM) advanced methods, with hydrodynamic modeling for dissipative properties, and, in the case of bis-labeled systems, with determination of dipolar interaction based on the molecular structures beyond the point-dipole approximation, are the fundamental ingredients needed by the SLE to provide a fully integrated computational approach (ICA) to the spectral profile.^{11,15} ICA has been already applied to the interpretation of continuous-wave ESR (cw-ESR) spectroscopy of peptides in different solvents and temperatures.^{16,17}

In this work, we use ICA to interpret the cw-ESR spectra in acetonitrile (MeCN) at 293 K of the doubly spin-labeled peptide Fmoc–Aib–TOAC–(Aib)₅–TOAC–Aib–OMe (NONA_{2,8}) (Fmoc: fluorenyl-9-methoxycarbonyl; Aib: α -aminoisobutyric acid; OMe: methoxy) and of the singly spin-labeled peptide Fmoc–Aib–TOAC–Aib–OMe (TRI₂) with both X-band (9 GHz) and W-band (95 GHz) ESR. We also extend our approach to interpret the cw-ESR spectra in frozen MeCN at 80 K of NONA_{2,8} and the singly spin-labeled peptide Fmoc–(Aib)₈–TOAC–OMe (NONA₉) at X and W bands. Comparing experiments and simulations at two different measurement frequencies is advantageous because the intrinsically higher resolution attained by W-band ESR makes experimental spectra sensitive to a different motion regime. The non-natural Aib residue differs from protein amino acids in that it has two methyl groups linked to the α -carbon atom. The presence of *gem*-methyl groups reduces drastically the accessible region in the φ,ψ conformational space.^{18,19} Like TOAC, Aib residues are known to be strong helical formers in peptides, favoring α - or β -helices depending on main-chain length, peptide composition, position of the Aib residues in the sequence, and environmental conditions (temperature, solvent polarity, number of solvent–solute hydrogen bonds).

The paper is organized as follows: in section II, we describe the experimental procedures and methods including synthesis, chemical characterization, Fourier transform infrared (FT-IR) absorption and cw-ESR spectroscopies, and X-ray diffraction of the three peptides. Section III is dedicated to a short overview of the methods included in the ICA. Results and discussion are outlined in section IV.

II. EXPERIMENTAL SECTION

A. Peptide Synthesis and Characterization. Peptides TRI₂, Fmoc–(Aib)₉–OMe (NONA), NONA₉, NONA_{2,8}, and the related octamer Fmoc–TOAC–(Aib)₇–OMe (OCTA₁), used to infer the 3D structure of the other peptides from its X-ray diffraction analysis (see below), were synthesized in solution by taking advantage of (i) the 1-(3-dimethylamino)propyl-3-ethylcarbodiimide (EDC), the EDC/1-hydroxy-1,2,3-benzotriazole (HOBr)²⁰ or the EDC/7-aza-1-hydroxy-1,2,3-benzotriazole (HOAt)²¹ method for the formation of the Aib–Aib bonds; and (ii) the EDC/HOAt or the carboxylic fluoride²² method for the formation of the TOAC–Aib and Aib–TOAC bonds. The chromatographically pure compounds exhibit the following physical

and analytical data: (a) TRI₂: melting point (m.p.) 96–98 °C (from ethyl acetate – petroleum ether); IR (KBr) 3330, 1739, 1682, 1524 cm^{−1}; mass spectrometry (MS) (ESI-TOF) [M+H]⁺ 622.34 for a calculated molecular weight (MW_{calcd}) 621.33. (b) OCTA₁: mp 201–203 °C (purified using flash chromatography and a dichloromethane–ethanol solvent mixture); IR (KBr) 3320, 1737, 1662, 1529 cm^{−1}; MS (ESI-TOF) [M+H]⁺ 1047.62 for a MW_{calcd} 1047.59. (c) NONA₉: mp 159–161 °C (purified as described above for TRI₂); IR (KBr) 3323, 1738, 1662, 1529 cm^{−1}; MS (ESI-TOF) [M+H]⁺ 1132.63 for a MW_{calcd} 1132.65. (d) NONA_{2,8}: mp 166–168 °C (purified as described above for TRI₂); IR (KBr) 3323, 1744, 1655, 1530 cm^{−1}; MS (ESI-TOF) [M+H]⁺ 1244.63 for a MW_{calcd} 1244.72. (e) NONA: mp 219–220 °C (purified as described above for TRI₂); IR (KBr) 3295, 1735, 1703, 1656, 1534 cm^{−1}; MS (ESI-TOF) [M+H]⁺ 1020.52 for a MW_{calcd} 1020.57.

B. FT-IR Absorption Spectroscopy. FT-IR absorption spectra were recorded using a Perkin-Elmer 1720 X FT-IR spectrophotometer, nitrogen-flushed, with a sample shuttle device and at 2 cm^{−1} nominal resolution, averaging 100 scans. Solvent (baseline) spectra were recorded under the same conditions. Cells with CaF₂ windows and path lengths of 0.1 and 1.0 mm were used. Spectrograde deuteriochloroform (99.8%, *d*) was obtained from Fluka.

C. ESR Spectroscopy. The cw-EPR spectra were recorded both at room temperature and in frozen solution using the Bruker Elexsys 680 (Bruker BioSpin GmbH, Rheinstetten, Germany) spectrometer.

The X-band (9.5 GHz) EPR measurements were performed in a rectangular cavity. At room temperature, a modulation frequency of 100 kHz and modulation amplitude of 20 μT (0.2 G) were applied. The samples were measured in Blueband 50 μ L pipettes. All samples were prepared in acetonitrile (purity 99.5%). The concentrations of mono- and biradical peptides were 0.5 mM and 0.25 mM, respectively. For the frozen solution measurements, both NONA₉ and NONA_{2,8} samples were diluted with NONA at a 10:1 NONA/NONA₉ or NONA/NONA_{2,8} ratio. The microwave power, modulation frequency, and modulation amplitude were 0.159 mW, 100 kHz, and 0.2 mT (2 G), respectively. The samples were prepared in 4 mm o.d. quartz tubes. The concentration of the TOAC peptide in the samples was always 0.1 mM.

For room-temperature W-band (95 GHz) measurements, a modulation frequency of 100 kHz and modulation amplitude of 0.1 mT (1 G) were applied. The concentration of mono- and biradical peptides was 2 mM and 1 mM, respectively. The samples were placed in suprasil quartz capillaries, with an inside diameter (i.d.) of 0.125 mm and outside diameter (o.d.) of 0.25 mm, from Wilmad-Labglass (Buena, NJ, USA). The capillaries were sealed at one end. A Wilmad suprasil quartz tube with an i.d. of 0.60 mm and an o.d. of 0.84 mm, which was sealed at one end, was used as an outside tube. The standard W-band sample clamp was used with the usual sample holder to place the sample properly in the resonator. For low-temperature W-band measurements, both NONA₉ and NONA_{2,8} samples were diluted with NONA in the ratios used for the X-band samples. The solutions were measured in Wilmad suprasil quartz tubes with an i.d. of 0.60 mm and an o.d. of 0.84 mm that were sealed at one end.

The samples were prepared directly in the Wilmad suprasil quartz tube with an i.d. of 0.60 mm and an o.d. of 0.84 mm, which was sealed at one end. For these frozen solution measurements,

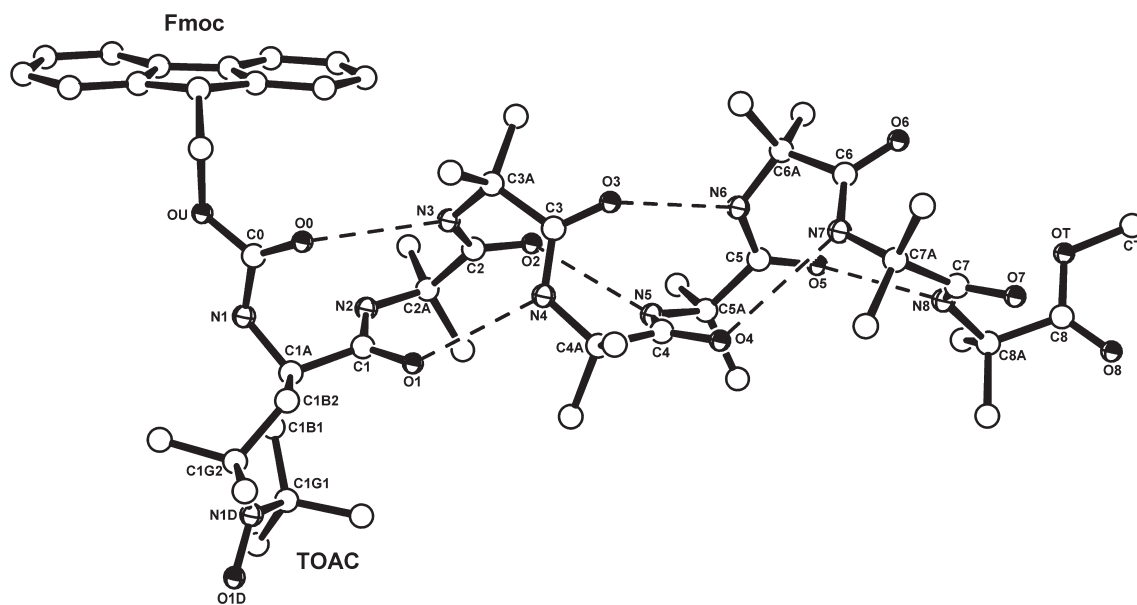


Figure 1. X-ray diffraction structure of the OCTA₁ molecules. The Fmoc- and TOAC-ring moieties are highlighted. Intramolecular H-bonds are represented by dashed lines.

the microwave power, modulation frequency, and modulation amplitude were 5.0×10^{-5} mW, 100 kHz, and 0.5 mT (5 G), respectively.

D. X-ray Diffraction. Single crystals of OCTA₁ were grown by slow evaporation from a methanol solution. Formula C₅₄H₈₀N₉O₁₂, $M = 1047.27$, monoclinic, space group P2₁/c, unit cell dimensions $a = 16.086(3)$ Å, $b = 21.066(3)$ Å, $c = 18.104(3)$ Å, $\beta = 100.27(7)^\circ$; $V = 6036.6(17)$ Å³, $Z = 4$; $d_{\text{calc}} = 1.152$ g cm⁻³. Crystal size and color: $0.40 \times 0.25 \times 0.15$ mm³, pale yellow. Absorption coefficient ($\text{CuK}\alpha$) = 0.670 mm⁻¹. Intensity data were collected at room temperature with CuK α radiation ($\lambda = 1.54178$ Å) using a Philips PW 1100 diffractometer in the $\theta - 2\theta$ scan mode up to $\theta = 54.2^\circ$ (0.95 Å resolution). The crystal did not significantly diffract at higher resolution. The structure was solved by direct methods with the SIR 2002 program.²³ Refinement was carried out by least-squares procedures on F^2 , using all data, by application of the SHELXL 97 program.²⁴ All non-hydrogen atoms were refined anisotropically. The aromatic rings of the N-terminal Fmoc group were constrained to the idealized geometry. Hydrogen atoms were calculated at idealized positions and refined using a riding model. The final R indices were $R_1 = 0.0864$, $wR_2 = 0.2244$ [$I > 2\sigma(I)$], and $R_1 = 0.1233$, $wR_2 = 0.2382$ (all data). Data/parameters: 7362/652. Goodness of fit on F^2 : 1.213. The largest peak and hole in the final difference Fourier map were 0.307 and -0.314 e Å⁻³, respectively. The final structure is shown in Figure 1. Crystallographic data (including atomic coordinates, bond distances, bond angles, torsion angles, intra- and intermolecular H-bond parameters) may be found in the Supporting Information as a CIF file. These data are also available from the Cambridge Crystallographic Data Centre, via www.ccdc.cam.ac.uk/data_request/cif, under deposition number CCDC-824745.

III. MODELING

ESR spectroscopy in the slow-motion regime can be interpreted effectively within the standard SLE approach,⁶ by taking into account structural, dynamical, and magnetic properties of

the molecular system under investigation. All these aspects are described by suitable input parameters, comprising basic molecular information and solvent macroscopic parameters. In this section, we give a brief description of the integrated approach to model cw-ESR in fluid phases. Details can be found elsewhere.^{11,15} Several ingredients are included in the ICA, namely, (i) QM/MM calculations, providing the structural and local magnetic properties of the system under investigation; (ii) calculation of dissipative parameters, such as rotational diffusion tensors, using standard hydrodynamics arguments; and (iii) computation of the electron exchange and dipolar interactions in the case of multiply labeled systems. Data generated by the mentioned methods enter in the parametrization of the SLE that describes the time evolution of the density matrix of the system, ρ , controlled by a stochastic operator, $\hat{\Gamma}$, and the spin Hamiltonian, \hat{H} ,⁹

$$\begin{aligned} \frac{\partial \rho(\sigma, \mathbf{q}, t)}{\partial t} &= -\hat{L}\rho(\sigma, \mathbf{q}, t) \\ &= -i[\hat{H}(\sigma, \mathbf{q}), \rho(\sigma, \mathbf{q}, t)] - \hat{\Gamma}(\mathbf{q})\rho(\sigma, \mathbf{q}, t) \quad (1) \end{aligned}$$

where σ represents the spin pseudocoordinates and \mathbf{q} is the set of stochastic coordinates.

Here, we treat the molecule as a rigid rotator freely reorienting in space. This treatment can be seen as a rather oversimplification of the whole dynamics of the system, but it showed to be sufficient to catch the relevant dynamical aspects affecting cw-ESR spectra in similar systems.^{16,17} Thus, in this case, the set of stochastic coordinates reduces to $\mathbf{q} = \Omega$, which are the three Euler angles describing the rotation from the inertial laboratory frame (LF) to the molecule-fixed frame (MF), where the rotational diffusion tensor, \mathbf{D} , is diagonal. The stochastic operator takes the form of the standard Smoluchowski operator:

$$\hat{\Gamma} = \hat{\mathbf{J}}(\Omega) \cdot \mathbf{D} \cdot \hat{\mathbf{J}}(\Omega) \quad (2)$$

where $\hat{\mathbf{J}}(\Omega)$ is the (body) angular momentum operator. Both $\hat{\Gamma}$ and \mathbf{D} are defined in the MF.

The spin Hamiltonian for the general case with two TOAC residues reads

$$\hat{H} = \frac{\beta_e}{\hbar} \sum_{i=1}^2 \mathbf{B}_0 \cdot \mathbf{g}_i \cdot \hat{\mathbf{S}}_i + \gamma_e \sum_{i=1}^2 \hat{\mathbf{I}}_i \cdot \mathbf{A}_i \cdot \hat{\mathbf{S}}_i - 2\gamma_e J \hat{\mathbf{S}}_1 \cdot \hat{\mathbf{S}}_2 + \hat{\mathbf{S}}_1 \cdot \mathbf{T} \cdot \hat{\mathbf{S}}_2 \quad (3)$$

where the first term is the Zeeman interaction of each electron spin with magnetic field \mathbf{B}_0 depending on the \mathbf{g}_i tensor; the second term is the hyperfine interaction of each ^{14}N nucleus with the unpaired electron, defined with respect to hyperfine tensor \mathbf{A}_i ; the third and fourth terms are, respectively, the electron exchange term, with exchange energy J , and spin–spin dipolar term, with the dipolar tensor \mathbf{T} . Here, tensors \mathbf{g}_i and \mathbf{A}_i are diagonal in the same local frame T_iF rigidly fixed on the i th TOAC nitroxide and defined with respect to MF by a set of angles Ω_i . Operators $\hat{\mathbf{I}}_i$ and $\hat{\mathbf{S}}_i$ are defined in the LF.

The SLE integrates the structural and dynamic ingredients to directly give the spectral density:

$$G(\Delta\omega) = \frac{1}{\pi} \mathcal{R}e \{ \langle v | [i\Delta\omega + (i\hat{H}^\times + \hat{\Gamma})]^{-1} | v P_{eq} \rangle \} \quad (4)$$

where $\hat{H}^\times = [\hat{H}, \dots]$ and $|v\rangle = (2I_1+1)^{-1}(2I_2+1)^{-1}(|\hat{S}_{X,1}\rangle + |\hat{S}_{X,2}\rangle)$, with I_i being the total spin moment of the i th nucleus. In eq 4 the equilibrium distribution is a constant because of the isotropy of the medium, i.e., $P_{eq} = 1/8\pi^2$.

The whole procedure allows the calculation of the spectral density with minimal resort to additional fitting procedures. Let us point out that, in conventional spectra simulation, the two steps of guessing the magnetic parameters and simulating the spectral profile are completely disentangled. On the contrary, our approach requires self-consistency between magnetic and diffusive parameters, which are both related to the structure issuing from *a priori* geometry optimization and/or short-time dynamics.

As mentioned in the Introduction, in this work we also calculate the cw-ESR spectra of the peptides in frozen MeCN, at 80 K. Since this temperature is far below the melting point of MeCN (equal to 227 K), it is possible to describe the spectrum as a powder distribution. The latter is obtained by calculating the static ESR spectra, using eq 4 without the stochastic term, for all of the orientations of the molecule with respect to the magnetic field \mathbf{B}_0 and then integrating over the solid angle.²⁵ The interpretation of the ESR powder spectra is then only based on the determination of the spin Hamiltonian parameters and molecular geometry. As shown in the next Section, to improve the agreement of the theoretical to experimental spectra for the NONA_{2,8} molecule, we take into account the distribution of the relative distance and orientation of the two TOAC residues. This requirement is imposed by the high sensitivity that powder spectra show with respect to the dipolar interaction of the two unpaired electrons (and thus to the molecular conformation), even if the two probes are about 12 Å and 14 Å far away, respectively, in the 3_{10}^- - and α -helices. Small deformations of the peptide backbone chain can lead to relevant changes in the relative conformation of the two TOAC residues with an important effect on the dipolar contribution. We shall define $\mathbf{Q} = (\Omega_1, \Omega_{1,2}, \mathbf{r}_{1,2})$ as the full set of coordinates, being a function of the backbone conformation, which includes the orientation of T_iF with respect to LF (Ω_1), the relative orientation of the two T_iF frames ($\Omega_{1,2}$) and the relative distance between the centers

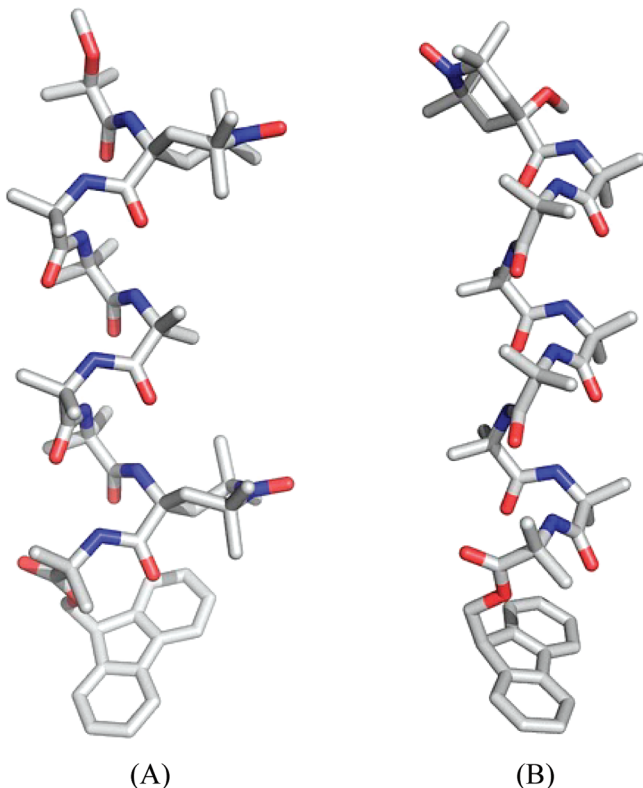


Figure 2. Optimized 3D-structures of (A) NONA_{2,8} and (B) NONA₉, viewed orthogonal to their helix axis.

of the two N–O moieties ($\mathbf{r}_{1,2}$). We assume that at 80 K backbone conformational changes are subject to high activation energies so that we can consider a static distribution of molecular conformations and calculate the spectrum as the following integral:

$$G(\Delta\omega) = d\mathbf{Q} G(\Delta\omega, \mathbf{Q}) P_{eq}(\mathbf{Q}) = \frac{1}{8\pi^2} \int d^3\Omega_1 d^3\Omega_{1,2} d^3\mathbf{r}_{1,2} G(\Delta\omega, \Omega_1, \Omega_{1,2}, \mathbf{r}_{1,2}) P_{eq}(\Omega_{1,2}, \mathbf{r}_{1,2}) \quad (5)$$

The average over the space of coordinates ($\Omega_{1,2}, \mathbf{r}_{1,2}$) can be substituted, via the ergodic hypothesis, with the time average over configurations obtained from a molecular dynamics (MD) trajectory, i.e.,

$$G(\Delta\omega, \Omega_1) \approx \frac{1}{\tau} \sum_{j=1}^N \Delta t G[\Delta\omega, \Omega_1, \Omega_{1,2}(j), \mathbf{r}_{1,2}(j)] \quad (6)$$

where Δt is the time step and $\tau = N\Delta t$ is the total length of the trajectory.

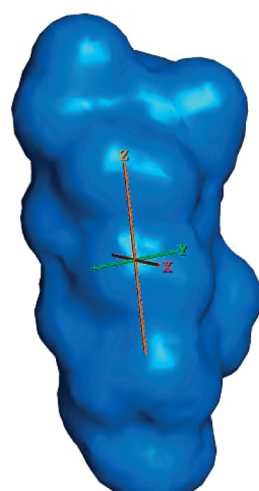
Integration over Ω_1 has been carried out by discretizing the angles over a grid and using the standard method of rectangles. Finally, to take into account any residual broadening of lines, the spectrum is convolved with a Gaussian function with adaptable (fitted) width.

IV. RESULTS AND DISCUSSION

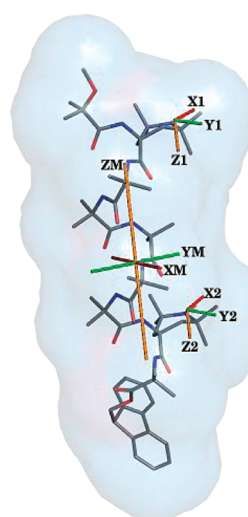
A. Conformational Analysis. We performed a conformational analysis of the TRI₂, OCTA₁, NONA₉, and NONA_{2,8} peptides in solution by the exclusive use of FT-IR absorption

Table 1. Principal Components of the g and A Tensors Used in the Simulations (Tensor Values A are Expressed in Gauss)

	room temperature spectra (293 K)				powder spectra (80 K)			
	NONA _{2,8}		TRI ₂		NONA _{2,8}		NONA ₉	
	X-band	W-band	X-band	W-band	X-band	W-band	X-band	W-band
<i>g</i> _{xx}	2.009	2.0096	2.009	2.0096	2.009147	2.009147	2.009147	2.009147
<i>g</i> _{yy}	2.006	2.0066	2.006	2.0066	2.006661	2.006661	2.006661	2.006661
<i>g</i> _{zz}	2.003	2.0036	2.003	2.0036	2.002694	2.002694	2.002694	2.002694
<i>A</i> _{xx}	5.39	5.39	5.67	5.67	6.85	6.85	6.85	6.85
<i>A</i> _{yy}	5.39	5.39	5.67	5.67	4.43	4.43	4.43	4.43
<i>A</i> _{zz}	33.87	33.87	33.67	33.67	36.0	36.0	36.0	36.0



(A)



(B)

Figure 3. Representation of the hydrodynamic surface for an effective radius of 2 Å with indication of the orientation of (A) diffusion tensor only and (B) diffusion tensor and magnetic frame principal axes for the NONA_{2,8} molecule.

spectroscopy since neither circular dichroism nor proton nuclear magnetic resonance are appropriate in these cases because all four compounds are achiral and contain at least one stable paramagnetic free radical. In the conformationally informative N–H stretching region, the FT-IR absorption spectrum of the shortest peptide in CDCl₃, a secondary-structure-supporting solvent, the trimer TRI₂, exhibits two bands: a weak one located at 3420 cm⁻¹ (free, solvated NH groups) and a slightly more intense one at 3360 cm⁻¹ (H-bonded NH groups).^{26,27} Here CDCl₃ is used as a secondary-structure supporting solvent. As the peptide main-chain length is elongated to the octa- and nonamer levels, the band at 3360 cm⁻¹ markedly moves to lower wavenumbers (3326–3320 cm⁻¹) and significantly increases in intensity.^{28,29} For the three long peptides, the ratios of the integrated molar extinction coefficients of the H-bonded versus free NH groups are strongly in favor of the onset of an almost fully developed 3₁₀-helical structure. Varying peptide concentration (below 1 × 10⁻³ M) changes the spectra only marginally.

The 3D-structure of OCTA₁ (the only peptide among the four synthesized in this work which gave single crystals in our hands), as determined by X-ray diffraction analysis, is illustrated in

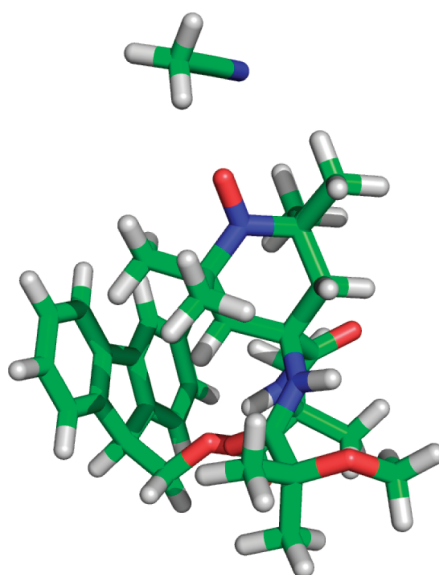
**Figure 4.** Optimized complex of TRI₂ with a MeCN molecule. Level of theory: PBE1PBE/6-311G(d,p).

Figure 1. As the peptide is achiral and crystallizes in a centrosymmetric space group, molecules of both handedness are found in the crystals. A molecule of the right-handed screw sense has been chosen as the asymmetric unit. The peptide backbone is folded into a regular 3₁₀-helix, stabilized by six consecutive intramolecular C=O · · · H–N H-bonds of the *i* → *i* + 3 type. Surprisingly, the C-terminal Aib(8) residue, although external to the H-bonding pattern, adopts a helical conformation with the same screw sense as that of the preceding residues.^{18,19} The piperidinyl ring of the TOAC residue is oriented roughly perpendicular to the helix axis, and to the aromatic system of the Fmoc group as well. The angle between normals to the average planes of the fluorene and the piperidinyl rings is 83.1(1)^o.

The piperidinyl ring of the TOAC residue is found in the ⁶T₂ twist conformation (relative to the ring atom sequence N^δ-C^{γ2}-C^{β2}-C^α-C^{β1}-C^{γ1}, where C^{β1} refers to the pro-(S) C^β atom). For a statistical analysis of TOAC ring conformations in the crystal state, see ref 30. The puckering parameters are the following: Q_T = 0.657(6) Å, φ₂ = 90.9(S)^o, θ₂ = 89.9(S)^o.³¹

In the packing mode, peptide molecules are linked head-to-tail through two intermolecular H-bonds, between the N–H groups of TOAC(1) and Aib(2) and the carbonyl oxygen atoms of Aib(7) and Aib(8), respectively, of a (1 + *x*, 1/2 – *y*, 1/2 + *z*)

Table 2. A_{iso} Values for Different QM Calculations *in Vacuo*, and in Implicit or Explicit Solvent^a

	A_{iso} /Gauss
<i>in vacuo</i> , B3LYP/N07D	13.74
implicit solvent, B3LYP/N07D/PCM	14.78
explicit solvent, B3LYP/N07D	15.32
explicit solvent, B3LYP/N07D/PCM	15.78
experimental value at 293 K	14.88
experimental value at 80 K	15.76

^a All QM computations were performed on the TRI_2 molecule. Experimental values were obtained from the experimental cw-ESR spectra of TRI_2 (293 K) and $\text{NONA}_{2,8}$ (80 K).

symmetry related molecule, giving rise to rows of molecules along the *ac* direction.

The fully optimized 3D structures of $\text{NONA}_{2,8}$, NONA_9 , and TRI_2 were obtained by PBE0/6-31G(d) calculations in the gas phase. Both the $\text{NONA}_{2,8}$ (Figure 2A) and NONA_9 (Figure 2B) peptide backbones are folded into a regular 3_{10} -helix, stabilized by six consecutive intramolecular $\text{C}=\text{O}\cdots\text{H}-\text{N}$ H-bonds of the $i \leftarrow i+3$ type. The average φ , ψ values are around $\pm 60^\circ$, $\pm 20^\circ$ for both structures (with differences in the absolute values less than 1°). In the $\text{NONA}_{2,8}$ structure, the piperidinyl rings of the two TOAC residues are oriented roughly perpendicular to the helix axis and parallel to each other. The piperidinyl rings are in the twist conformation, and the average distance between the nitroxide $\text{N}\cdots\text{N}$ and $\text{O}\cdots\text{O}$ atoms is 11.96 Å. A similar 3_{10} -helical structure was determined a few years ago by Gessmann et al.³² using X-ray diffraction for a terminally protected $-(\text{Aib})_9-$ sequence.

Simulation of the ESR spectra requires the employment of a suite of integrated programs for the prediction of the different system parameters/properties: (a) DFT calculations are the basis of the entire simulation protocol because they provide all information that enters, as subsequent input, all of the remaining program codes. The main information obtained from the DFT study is relative to structural properties of the molecule. (b) The calculation of the diffusion tensor is based on the geometry obtained from QM calculations using a hydrodynamic approach. (c) Electronic information obtained from step (a) is also fed to the dipolar interaction tensor evaluation procedure. All data from (a) and (b) enter, as input parameters, in the program that calculates the ESR spectra based on the SLE, which is the last step. Table 1 summarizes all parameters employed in the final step.

B. Dissipative Properties. The diffusion tensors, \mathbf{D} , of the TRI_2 and $\text{NONA}_{2,8}$ molecules have been evaluated with the hydrodynamics-based approach outlined in refs 12–14. The molecule is described as a set of N rigid fragments made of atoms or groups of atoms immersed in a homogeneous isotropic fluid of known viscosity. The tensor \mathbf{D} can be conveniently partitioned into translational, rotational, internal, and mixed blocks. It is obtained as the inverse of the friction tensor, Ξ , using Einstein's relation^{12,13}

$$\mathbf{D} = \begin{bmatrix} \mathbf{D}_{\text{TT}} & \mathbf{D}_{\text{TR}} & \mathbf{D}_{\text{TI}} \\ \mathbf{D}_{\text{TR}}^{\text{tr}} & \mathbf{D}_{\text{RR}} & \mathbf{D}_{\text{RI}} \\ \mathbf{D}_{\text{TI}}^{\text{tr}} & \mathbf{D}_{\text{RI}}^{\text{tr}} & \mathbf{D}_{\text{II}} \end{bmatrix} = k_{\text{B}} T \Xi^{-1} \quad (7)$$

where k_{B} is the Boltzmann constant and T is the absolute temperature. The friction tensor for the constrained system of spheres

(the real molecule), Ξ , is calculated for the friction tensor of nonconstrained extended atoms, ξ , as pointed out in refs 12–14. In our case, the complete diffusion tensor is represented by a 6×6 matrix. Due to the translational invariance of the magnetic tensors, one may project out the translational part and reduce the diffusion tensor to a 3×3 matrix made up only of the rotational tensor, $\mathbf{D} = \mathbf{D}_{\text{RR}}$. Figure 3A shows the $\text{NONA}_{2,8}$ molecule as a group of spheres rigidly attached constituting a body free to reorient in the isotropic medium. The size and shape of this body are related not only to the shape of the molecule, but also to the choice of the effective hydrodynamic radius associated with the extended atoms. Figure 3B shows the molecular structure of $\text{NONA}_{2,8}$ with the indication of magnetic frames.

For both TRI_2 and $\text{NONA}_{2,8}$ molecules, the diffusion tensors have been calculated with this set of parameters: viscosity 0.37 cP,^{33,34} temperature 293 K, an effective radius of 2 Å for the atoms and stick boundary conditions. Principal values of the diffusion tensor of TRI_2 are $D_{\text{XX}} = 2.0 \times 10^9$, $D_{\text{YY}} = 2.2 \times 10^9$ and $D_{\text{ZZ}} = 2.8 \times 10^9 \text{ s}^{-1}$, while for $\text{NONA}_{2,8}$ we find $D_{\text{XX}} = 5.5 \times 10^8$, $D_{\text{YY}} = 5.6 \times 10^8$ and $D_{\text{ZZ}} = 14.9 \times 10^8 \text{ s}^{-1}$.

C. QM Calculations of A_{iso} . For the calculation of cw-ESR spectra at 293 K, we employed values for both the \mathbf{g} and \mathbf{A} tensors calculated for a similar system: a heptapeptide based on Aib and TOAC residues, in MeCN.¹⁷ Some difficulties were encountered in the simulations at 80 K. From the experimental spectra it is clear that the values of the isotropic part (A_{iso}) and the A_{ZZ} component of the hyperfine coupling tensor drastically change with temperature. In particular, both values are lower at 293 K. This behavior could be explained by taking into account the trend of dielectric constant of MeCN with temperature. It ranges from 36.8 at 293 K to 47.1 at 233 K.³⁵ The dependence of the hyperfine and \mathbf{g} -tensor parameters of nitroxides on temperature and environment was observed earlier.^{36–38} As an illustration, Owenius et al.³⁹ showed that A_{iso} increases nonlinearly as the dielectric constant is enhanced. Increments are between 0.7 and 1.5 G for a dielectric constant higher than 30. Similarly, A_{ZZ} shows an increasing trend as the dielectric constant increases. The variation of A_{ZZ} spans over a range of 3 G. Another possible explanation could be the presence of a specific TOAC-(NO)-MeCN interaction that becomes relevant only at low temperature (when thermal agitation of the solvent molecules is low). We shall use QM calculations to test this second hypothesis.

We tried to reproduce via QM calculations the 80 K values of A_{iso} , using the optimized structure of TRI_2 . The experimental value in frozen solution is equal to 15.76 G. Calculations were performed under different conditions: vacuum, implicit solvent (PCM), and explicit solvent. All the QM calculations were performed with the Gaussian 09 software.⁴⁰ TRI_2 was fully optimized *in vacuo* at PBE1PBE/6-311G(d,p) level of theory.⁴¹ For the A_{iso} value *in vacuo*, calculated with the B3LYP functional and basis set N07D,⁴² we obtained 13.74 G. Solvent effects in QM calculation were accounted for using implicit and explicit solvent methods. The polarizable continuum model (PCM)⁴³ was employed to include implicit solvent effects. A standard cavity was used, and the dielectric constant of MeCN employed was 35.69. An enhancement of A_{iso} was obtained, to the new value of 14.78 G. This result is in very good agreement with the experimental A_{iso} , which is equal to 14.88 G.

To test the hypothesis of a specific TOAC(NO)-MeCN interaction being relevant at 80 K, we repeated the DFT calculations with the addition of one solvent molecule. The small

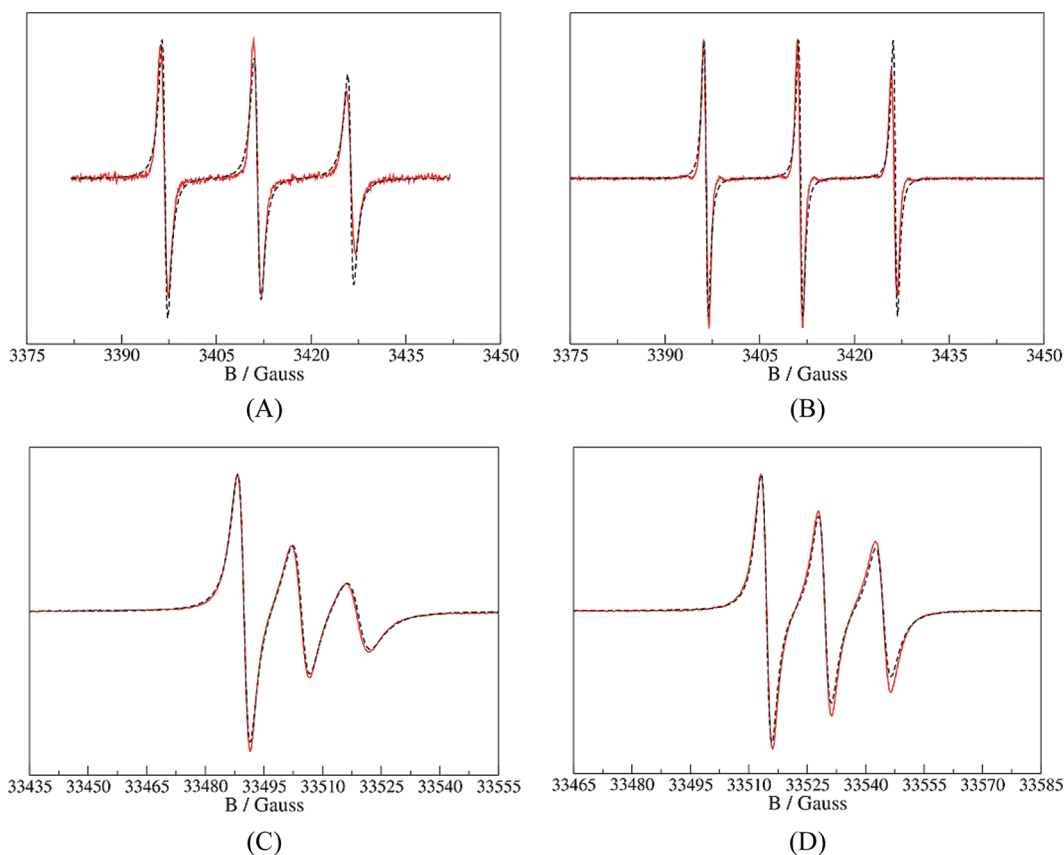


Figure 5. Simulated (black dashed line) and experimental (red continuous line) spectra of $\text{NONA}_{2,8}$ (left side) and TRI_2 (right side) in MeCN at 293 K for X-band (A,B) and W-band (C,D).

system composed by TRI_2 and one MeCN molecule was fully optimized *in vacuo* at the PBE1PBE/6-311G(d,p) level of theory (Figure 4). The distance between the TOAC oxygen atom and the nearest methyl hydrogen atom is 2.18 Å. This value is close to other QM calculations on similar systems.⁴⁴ Then, using the minimum energy configuration, we calculated the hyperfine coupling constant at DFT level with the B3LYP functional and the N07D basis set. A_{iso} changes radically to 15.32 G *in vacuo*, with a small correction to 15.78 G when the PCM correction is also used. The latter value is in excellent agreement with the experimental constant that can be extracted from powder spectra, which is 15.76 G. This agreement confirms the hypothesis that in the frozen solution the solute···solvent specific interaction (hydrogen bond) at the level of the N–O moiety has an important effect on the ^{14}N – electron hyperfine coupling. Moreover, it can be hypothesized that thermal effects at high temperature make the specific interaction more difficult to persist, and only bulk effects (simulated with the PCM model) are important. Table 2 reports a summary of all results obtained with the different QM calculations.

D. MD Calculations. MD simulations of the bis-labeled peptide ($\text{NONA}_{2,8}$) at 80 K were employed to gain specific information about the geometry and stability of the secondary structures (3_{10} - and α -helices). In our simulations with the AMBER10⁴⁵ package, the initial positional coordinates were taken from an optimized MM structure. The MD simulations were carried out with the *sander* module using a modified ff99SB force field. Parameters for the non-natural Aib residue were taken from the *resp esp charge database* (REDDB),⁴⁶ while force field

parameters for the TOAC residue were derived from a parametrization of nitroxide molecules recently presented by Barone and co-workers.⁴⁷ For the Fmoc cap we used standard parameters of the ff99SB force field. Finally, data for MeCN were obtained from the Amber parameter database.⁴⁸ We studied the peptide in the two types of helical conformations and performed simulations both *in vacuo* and in solvent.

The first run, *in vacuo* at 80 K, showed a very fast conversion from α - to 3_{10} -helix within 100 ps. No other transition was observed in the 1 ns-long calculated trajectory. This result is compatible with the fact that Aib residues favor the 3_{10} -helical geometry.

For the simulations in explicit solvent, we investigated the system with the peptide in the α -helix conformation in the interior of a 44.3 Å × 44.3 Å × 37.3 Å box, surrounded by 385 MeCN molecules. Moreover, the peptide in 3_{10} -helix conformation was placed in the interior of a 56.7 Å × 44.3 Å × 32.7 Å box, surrounded by 425 MeCN molecules. In both cases, periodic boundary conditions were applied. We followed the standard protocol starting with 2000 steps of energy minimization, 1500 with the steepest descent algorithm, and the remaining 500 steps with the conjugate gradient method. A 10 Å cutoff for the nonbonded interactions was used. Then, a short run of 100 ps was used to heat the system to 80 K. Finally, a 3 ns trajectory was produced, using a 1 fs time step of integration and saving the state of the system every 0.1 ps. The first two ns of the trajectory were dropped as equilibration time.

We observed no secondary structure change during the explicit solvent simulations. This result suggests a high energy

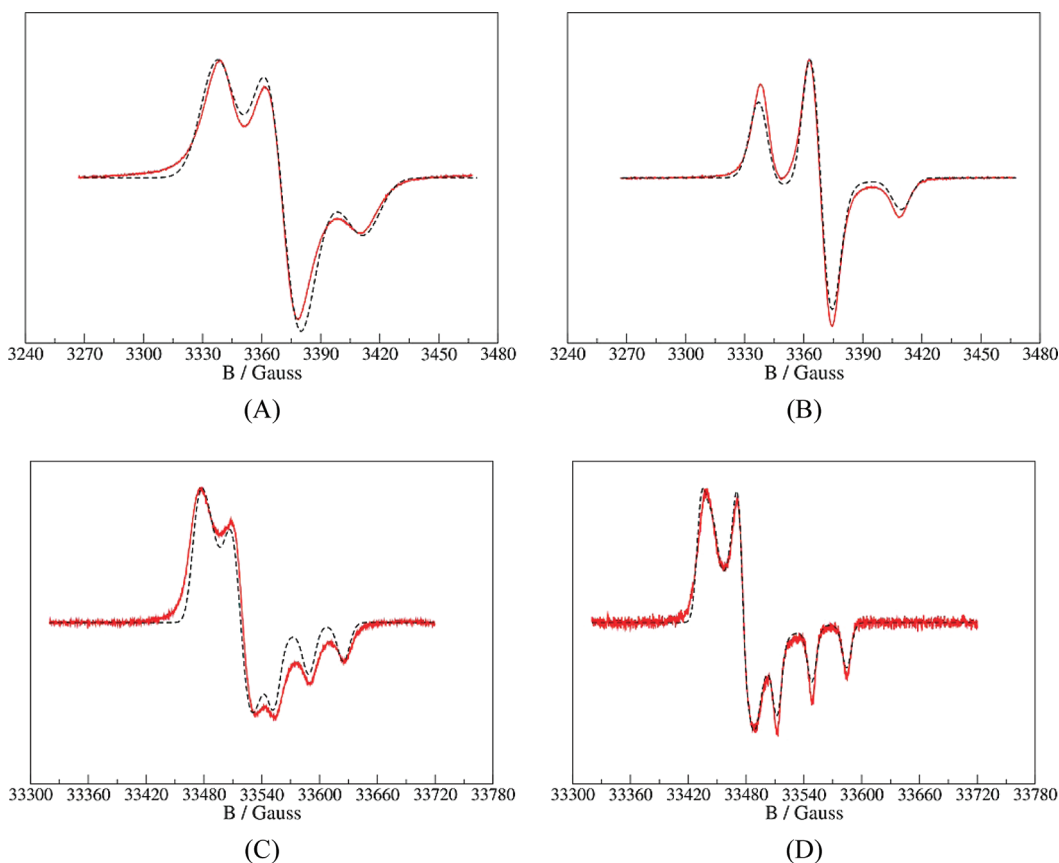


Figure 6. Simulated (black dashed line) and experimental (red continuous line) spectra of NONA_{2,8} (left side) and NONA₉ (right side) in MeCN at 80 K for X-band (A,B) and W-band (C,D).

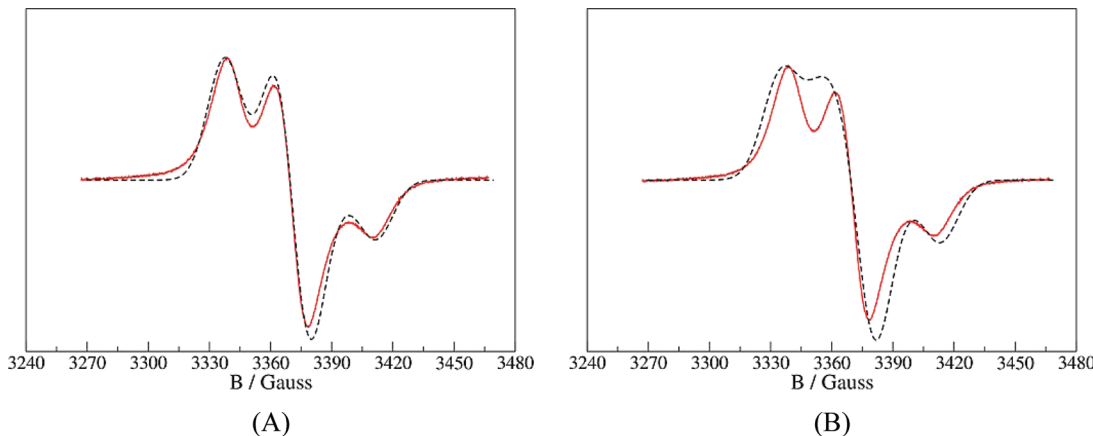


Figure 7. Comparison between theoretical (black dashed line) and experimental (red continuous line) X-band spectra in MeCN at 80 K for the (A) α - and (B) 3_{10}^{h} -helical conformations of NONA_{2,8}.

barrier for this specific 3_{10}^{h} - to α -helix transition probably related to the joint effect of stabilization of the peptide structures due to solute–solvent interactions and high energy in changing the structure of the MeCN molecules around the peptide.

E. Simulation of the cw-ESR Spectra. Room-Temperature Spectra Calculations. The set of values used in the simulations of the X-band cw-ESR spectra of NONA_{2,8} and TRI₂ at room temperature are summarized in Table 1. The values are the same as those obtained from QM calculations (DFT method) carried

out in a similar system.¹⁷ For the NONA_{2,8} molecule, the set of Euler angles specifying the rotation from MF to T_F are $\alpha = 60^\circ$, $\beta = 15.5^\circ$ and $\gamma = 0^\circ$. The exchange term, J , can be thought to be negligible, given the large distance of the two nitroxides and the presence of only three well-defined peaks in the experimental X-band spectrum. Our attempts to fit J resulted in very small values (<2 G in absolute value) with no significant improvement in the agreement between theoretical and experimental spectra. Therefore, we decided to set J to 0 G. About the dipolar

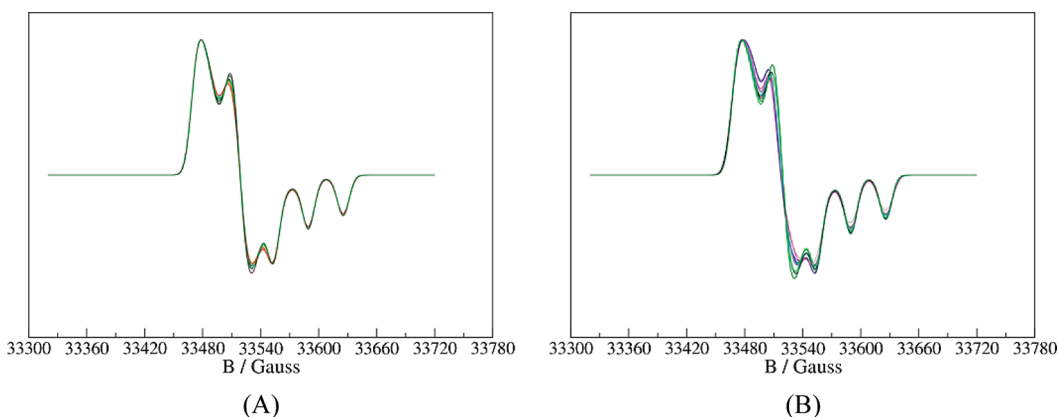


Figure 8. Theoretical W-band spectra in MeCN at 80 K for NONA_{2,8} in the (A) α - and (B) 3₁₀^o-helical conformations, obtained from selected MD snapshots taken every 100 ps.

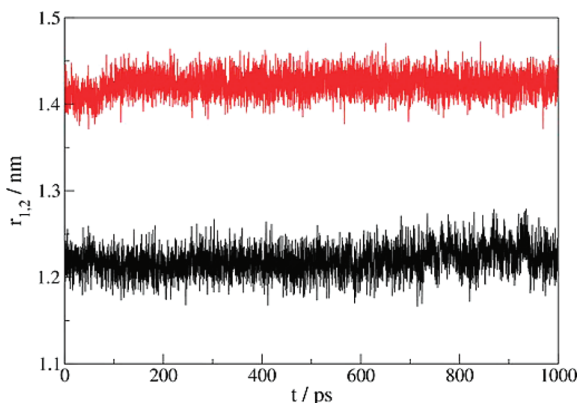


Figure 9. Time dependence of the intramolecular distance between the two N–O groups in the α - (red line) and 3_{10} - (black line) helices.

interaction, the two nitroxides are sufficiently far away such that the point-dipole approximation is valid (Figure 7 of ref 16). Thus, elements of the dipolar tensor are given by the standard expression

$$T_{\alpha\beta} = \frac{\mu_0}{4\pi} \frac{g_e^2 \beta_e^2}{h r_{1,2}^3} \left[\delta_{\alpha,\beta} - \frac{(\mathbf{r}_{1,2})_\alpha (\mathbf{r}_{1,2})_\beta}{r_{1,2}^2} \right] \quad (8)$$

where μ_0 is the vacuum magnetic permeability, g_e is the free electron g value, β_e is the electron Bohr magneton, $r_{1,2} = ||\mathbf{r}_{1,2}||$, and $\alpha, \beta = X, Y, Z$.

The comparison between simulated and experimental X-band spectra of NONA_{2,8} in MeCN at room temperature (293 K) is shown in Figure 5A.

Analogously, we simulated the ESR spectra of TRI_2 for which input parameters are reported in Table 1. The relative orientation between MF and $T_i\text{F}$ is given by $\alpha = 228^\circ$, $\beta = 51.6^\circ$, and $\gamma = 232^\circ$. Simulated and experimental X-band spectra are shown in Figure 5B. For both systems we used an intrinsic line width of 0.59 G.

For the simulations of the W-band cw-ESR spectra of $\text{NONA}_{2,8}$ and TRI_2 at room temperature we employed the same set of principal values and orientations of magnetic tensors (Table 1) used in the X-band simulations. The calculated and experimental W-band spectra of $\text{NONA}_{2,8}$ and TRI_2 are shown in Figure 5C,D,

respectively. Intrinsic linewidths of 1.7 G (NONA_{2,8}) and 2.1 G (TRI₂) were used.

Powder Spectra Calculations. Principal values of the magnetic tensors employed in the powder spectra simulations of both NONA_{2,8} and NONA₉ are listed in Table 1. Because powder spectra are extremely sensitive to small variations of principal components of both g and A tensors, results from QM calculations are not usable as such. At present, QM predictions are in general sufficiently accurate for reproducing cw-ESR spectra in the fluid phase, but the level of accuracy is still not enough for powder spectra. Thus, we performed an analysis of the NONA₂ W-band spectrum to fit the g and A tensors, which were then used in all simulations. Table 1 reports the principal values obtained for g and A. The isotropic part of the hyperfine coupling tensor and its A_{ZZ} component are close to the values that can be read directly from the spectrum (36.04 G for NONA_{2,8} and 36.13 G for NONA₉, from the W-band spectrum). Also, the value $A_{iso} = 15.76$ G is close to the QM calculated value when an explicit solvent molecule is included (Table 2). A slight anisotropy in A_{XX} and A_{YY} is observed. This break-up of cylindrical symmetry of the hyperfine coupling tensor was measured also for other similar probes in highly orienting media.⁴⁹ The same set of parameters was used for simulating the remaining spectra. Comparison of experimental and theoretical spectra of NONA₂ at X- and W-bands are given, respectively, in Figure 6B,D. In both cases, an intrinsic line width of 6.7 G was employed.

Simulations of NONA_{2,8} were more challenging. As it was reported by different authors,⁵⁰⁻⁵³ powder spectra of biradicals are very sensitive to the dipolar interaction between the two unpaired electrons at a distance of 20 Å. Powder spectra are therefore sensitive to molecular geometry, and this gives us the opportunity to distinguish between the α - or 3₁₀-helical structures. In particular, we observe that X-band spectra are the most sensitive to secondary structure. This finding is emphasized by the simulations, which reveal that the α -helical structure is indeed present in frozen MeCN. Figure 6A shows the experimental and theoretical X-band spectra of NONA_{2,8}. A line width of 11.4 G was used in the simulation. Comparison of X-band spectra of NONA_{2,8} for the α - and 3₁₀-helix conformations are reported in Figure 7A,B, respectively. The large difference in the two simulated spectra confirms the sensitivity of X-band spectra to the molecular structure. This result is not observed for W-band

spectra, shown in Figure 6C, for which both α - and 3_{10} -helices reproduce the experimental line shape.

Notice that the best agreement between experimental and calculated spectra for NONA_{2,8}, in both X- and W-bands, was achieved by considering a distribution of relative conformations of the two TOAC residues due to the distribution of peptide backbone conformations, i.e., by averaging over snapshots taken from the MD trajectories (eq 6). We stress that here we consider the TOAC rings as rigid units, thus only the dipolar interaction is affected by peptide geometric fluctuations. Figure 8A,B shows the theoretical W-band spectra, respectively, for α - and 3_{10} -helices from 10 selected structures along the trajectory. It can be observed that the central part of the spectra is strongly affected by the geometry. Moreover, the 3_{10} -helix spectra show a larger fluctuation of line shape with respect to those of the α -helix. This is due to a shorter average intramolecular distance between the two N—O groups (Figure 9), which makes the spectrum more sensitive to the dipolar interaction. A shorter distance implies a higher dipolar interaction.

V. CONCLUSIONS

A combination of different computational techniques, ranging from MD, to QM-DFT calculations, to stochastic modeling has been employed to interpret cw-ESR spectra in order to assess the secondary structure and dynamic characteristics of multilabeled peptides of different lengths. Some refinement of calculated parameters is still required, as in the case of calculation of the magnetic tensors of powder spectra. However, the number of free parameters is limited, and the starting point is close enough to final values, so that convergence to the true minimum is obtained. By a careful usage of structural and dynamic molecular parameters obtained via different convergent computational techniques, the present integrated approach is able to interpret and rationalize cw-ESR spectra of relatively large molecular systems in nonprotic solvents starting, essentially, only from the 3D-structure of the solutes and the macroscopic solvent properties.

■ ASSOCIATED CONTENT

5 Supporting Information. File mc144.cif: structure of Fmoc—TOAC—(Aib)₇—OMe (Cambridge Crystallographic Data Centre, file number CCDC-824745). This material is available free of charge via the Internet at <http://pubs.acs.org>.

■ AUTHOR INFORMATION

Corresponding Author

*E-mail: antonino.polimeno@unipd.it. Phone: (+39) 049 8275146. FAX: (+39) 049 8275829.

■ ACKNOWLEDGMENT

S.C., M.Z., and A.P. acknowledge support provided by the Italian Ministero dell’Istruzione, Università e Ricerca (MIUR Grant No. PRIN2006_2006033728) and by the University of Padova (Grant “Progetto Strategico” HELIOS 2009).

■ REFERENCES

- (1) Hubbell, W. L.; Cafiso, D. S.; Altenbach, C. *Nat. Struct. Biol.* **2000**, *7*, 735.
- (2) Fajer, P. G. *J. Phys.: Condens. Matter* **2005**, *17*, S1459.
- (3) Longhi, S.; Belle, V.; Fournel, A.; Giugliarelli, B.; Carrière, F. *J. Pept. Sci.* **2011**, *17*, 315.
- (4) Flippin-Anderson, J. L.; George, C.; Valle, G.; Valente, E.; Bianco, A.; Formaggio, F.; Crisma, M.; Toniolo, C. *Int. J. Pept. Protein Res.* **1996**, *47*, 231.
- (5) Hanson, P.; Martinez, G.; Millhauser, G.; Formaggio, F.; Crisma, M.; Toniolo, C.; Vita, C. *J. Am. Chem. Soc.* **1996**, *118*, 271.
- (6) Hanson, P.; Millhauser, G.; Formaggio, F.; Crisma, M.; Toniolo, C. *J. Am. Chem. Soc.* **1996**, *118*, 7618.
- (7) Toniolo, C.; Benedetti, E. *Trends Biochem. Sci.* **1991**, *16*, 350.
- (8) Benedetti, E.; Di Blasio, B.; Pavone, V.; Pedone, C.; Toniolo, C.; Crisma, M. *Biopolymers* **1992**, *32*, 453.
- (9) Schneider, D. J.; Freed, J. H. *Adv. Chem. Phys.* **1989**, *73*, 387.
- (10) Polimeno, A.; Freed, J. H. *Adv. Chem. Phys.* **1992**, *83*, 89.
- (11) Barone, V.; Polimeno, A. *Phys. Chem. Chem. Phys.* **2006**, *8*, 4609.
- (12) Moro, G. *Chem. Phys.* **1987**, *118*, 167.
- (13) Moro, G. *Chem. Phys.* **1987**, *118*, 181.
- (14) Barone, V.; Zerbetto, M.; Polimeno, A. *J. Comput. Chem.* **2009**, *30*, 2.
- (15) Zerbetto, M.; Polimeno, A.; Barone, V. *Comput. Phys. Commun.* **2009**, *180*, 2680.
- (16) Zerbetto, M.; Carlotto, S.; Polimeno, A.; Zerbetto, M.; Corvaja, C.; Franco, L.; Toniolo, C.; Formaggio, F.; Barone, V.; Cimino, P. *J. Phys. Chem. B* **2007**, *111*, 2668.
- (17) Carlotto, S.; Cimino, P.; Zerbetto, M.; Franco, L.; Corvaja, C.; Crisma, M.; Formaggio, F.; Toniolo, C.; Polimeno, A.; Barone, V. *J. Am. Chem. Soc.* **2007**, *129*, 11248.
- (18) Karle, I. L.; Balaram, P. *Biochemistry* **1990**, *29*, 6747.
- (19) Toniolo, C.; Crisma, M.; Formaggio, F.; Peggion, C. *Biopolymers (Pept. Sci.)* **2001**, *60*, 396.
- (20) König, W.; Geiger, R. *Chem. Ber.* **1970**, *103*, 788.
- (21) Carpino, L. A. *J. Am. Chem. Soc.* **1993**, *115*, 4397.
- (22) Carpino, L. A.; Sadat-Aalaee, D.; Chao, H. G.; DeSelms, R. H. *J. Am. Chem. Soc.* **1990**, *112*, 9651.
- (23) Burla, M. C.; Camalli, M.; Carrozzini, B.; Cascarano, G. L.; Giacovazzo, C.; Polidori, G.; Spagna, R. *J. Appl. Crystallogr.* **2003**, *36*, 1103.
- (24) Sheldrick, G. M. *Acta Crystallogr. A* **2008**, *64*, 112.
- (25) Morin, G.; Bonnin, D. *J. Magn. Reson.* **1999**, *136*, 176.
- (26) Cung, M. T.; Marraud, M.; Néel, J. *Ann. Chim. (Paris)* **1972**, *183*.
- (27) Pysh, E. S.; Toniolo, C. *J. Am. Chem. Soc.* **1977**, *99*, 6211.
- (28) Toniolo, C.; Bonora, G. M.; Barone, V.; Bavoso, A.; Benedetti, E.; Di Blasio, B.; Grimaldi, P.; Lelj, F.; Pavone, V.; Pedone, C. *Macromolecules* **1985**, *18*, 895.
- (29) Pispisa, B.; Palleschi, A.; Stella, L.; Venanzi, M.; Mazzuca, C.; Formaggio, F.; Toniolo, C.; Broxterman, Q. B. *J. Phys. Chem. B* **2002**, *106*, 5733.
- (30) Crisma, M.; Deschamps, J. R.; George, C.; Flippin-Anderson, J. L.; Kaptein, B.; Broxterman, Q. B.; Moretto, A.; Oancea, S.; Jost, M.; Formaggio, F.; Toniolo, C. *J. Pept. Res.* **2005**, *65*, 564.
- (31) Cremer, D.; Pople, J. A. *J. Am. Chem. Soc.* **1975**, *97*, 1354.
- (32) Gessmann, R.; Brückner, H.; Kokkinidis, M. *Acta Crystallogr. B* **1998**, *54*, 300.
- (33) Yawada, Y.; Tsuneda, T.; Yanagisawa, S.; Yanai, T.; Hirao, K. *J. Chem. Phys.* **2004**, *120*, 8425.
- (34) Kamiya, M.; Sekino, H.; Tsuneda, T.; Hirao, K. *J. Chem. Phys.* **2005**, *122*, 234111.
- (35) Usacheva, T. M.; Lifanova, N. V.; Zhuravlev, V. I.; Novozhilov, A. A.; Matveev, V. K. *Zh. Fiz. Khim.* **2000**, *74*, 1962.
- (36) Bales, B. L.; Blum, R. A.; Mareno, D.; Peric, M.; Halpern, H. J. *J. Magn. Reson.* **1992**, *98*, 299.
- (37) Ondar, M. A.; Grinberg, O. Y.; Doubinskii, A. A.; Lebedev, Y. S. *Khim. Fiz.* **1984**, *3*, 527.
- (38) Bullock, A. T.; Howard, C. B. *J. Chem. Soc., Faraday Trans.* **1980**, *76*, 1296.

- (39) Owenius, R.; Engstrom, M.; Lindgren, M.; Huber, M. *J. Phys. Chem. A* **2001**, *105*, 10967.
- (40) Frisch, M. J.; Trucks, G. W.; Schlegel, H. B.; Scuseria, G. E.; Robb, M. A.; Cheeseman, J. R.; Scalmani, G.; Barone, V.; Mennucci, B.; Petersson, G. A.; Nakatsuji, H.; Caricato, M.; Li, X.; Hratchian, H. P.; Izmaylov, A. F.; Bloino, J.; Zheng, G.; Sonnenberg, J. L.; Hada, M.; Ehara, M.; Toyota, K.; Fukuda, R.; Hasegawa, J.; Ishida, M.; Nakajima, T.; Honda, Y.; Kitao, O.; Nakai, H.; Vreven, T.; Montgomery, Jr., J. A.; Peralta, J. E.; Ogliaro, F.; Bearpark, M.; Heyd, J. J.; Brothers, E.; Kudin, K. N.; Staroverov, V. N.; Kobayashi, R.; Normand, J.; Raghavachari, K.; Rendell, A.; Burant, J. C.; Iyengar, S. S.; Tomasi, J.; Cossi, M.; Rega, N.; Millam, N. J.; Klene, M.; Knox, J. E.; Cross, J. B.; Bakken, V.; Adamo, C.; Jaramillo, J.; Gomperts, R.; Stratmann, R. E.; Yazyev, O.; Austin, A. J.; Cammi, R.; Pomelli, C.; Ochterski, J. W.; Martin, R. L.; Morokuma, K.; Zakrzewski, V. G.; Voth, G. A.; Salvador, P.; Dannenberg, J. J.; Dapprich, S.; Daniels, A. D.; Farkas, Ö.; Foresman, J. B.; Ortiz, J. V.; Cioslowski, J.; Fox, D. J. *Gaussian 09*, revision A.1, Gaussian, Inc.: Wallingford, CT, 2009.
- (41) (a) Perdew, J. P.; Burke, K.; Ernzerhof, M. *Phys. Rev. Lett.* **1996**, *77*, 3865. (b) Perdew, J. P.; Burke, K.; Ernzerhof, M. *Phys. Rev. Lett.* **1997**, *78*, 1396. (c) Adamo, C.; Barone, V. *J. Chem. Phys.* **1999**, *110*, 6158.
- (42) Barone, V.; Cimino, P.; Stendardo, E. *J. Chem. Theory Comput.* **2008**, *4*, 751.
- (43) Tomasi, J.; Mennucci, B.; Cammi, R. *Chem. Rev.* **2005**, *105*, 2999.
- (44) Kryachko, E. S.; Nguyen, M. T. *J. Phys. Chem. A* **2002**, *106*, 4267.
- (45) Case, D. A.; Darden, T. A.; Cheatham, T. E., III; Simmerling, C. L.; Wang, J.; Duke, R. E.; Luo, R.; Crowley, M.; Walker, R. C.; Zhang, W.; Merz, K. M.; Wang, B.; Hayik, S.; Roitberg, A.; Seabra, G.; Kolossváry, I.; Wong, K. F.; Paesani, F.; Vanicek, J.; Wu, X.; Brozell, S. R.; Steinbrecher, T.; Gohlke, H.; Yang, L.; Tan, C.; Mongan, J.; Hornak, V.; Cui, G.; Mathews, D. H.; Seetin, M. G.; Sagui, C.; Babin, V.; Kollman, P. A. *AMBER 10*, University of California: San Francisco, CA, 2008.
- (46) Dupradeau, F. Y.; Cézard, C.; Lelong, R.; Stanislawiak, E.; Oecher, J.; Delepine, J. C.; Cieplack, P. *Nucleic Acid Res.* **2008**, D360.
- (47) Stendardo, E.; Pedone, A.; Cimino, P.; Menziani, M. C.; Crescenzi, O.; Barone, V. *Phys. Chem. Chem. Phys.* **2010**, *12*, 11697.
- (48) Grabuleda, X.; Jaime, C.; Kollman, P. A. *J. Comput. Chem.* **2000**, *21*, 901.
- (49) Freed, J. H. In *Spin Labeling Theory and Applications*; Berliner, L. J., Ed.; Academic Press: New York, 1976; pp 53–132.
- (50) Fu, Z.; Aronoff-Spencer, E.; Backer, J. M.; Gerfen, G. J. *Proc. Natl. Acad. Sci. U.S.A.* **2003**, *100*, 3275.
- (51) Steinhoff, H.-J. *Biol. Chem.* **2004**, *385*, 913.
- (52) Hustedt, E. J.; Beth, A. H. *Annu. Rev. Biophys. Biomol. Struct.* **1999**, *28*, 129.
- (53) Rabenstein, M. D.; Shin, Y. K. *Proc. Natl. Acad. Sci. U.S.A.* **1995**, *92*, 8239.